Identification and H∞ Robust Control of Wireless Power Transfer System by Hammerstein Model

Shuaiqi Li, Qijun Deng, Zhifan Li, Jiangtao Liu, Chang Yu, *Member, IEEE*, Kaicong Cui, and Peng Luo

***Abstract*—In the field of control-oriented modeling of wireless power transfer (WPT) system, it is urgent to establish a simple model to reflect the nonlinear characteristics introduced by phase-shift control methods, which is significant to the design of controllers. Due to the nonlinear nature introduced by phase-shift control, controllers designed based on specific steady-state small-signal models struggle to maintain closed-loop dynamic performance. In this article, the nonlinearities of the WPT system are implicitly considered by using the Hammerstein model-based identification (HMI) method, so the accuracy of the identified model is guaranteed even if the working point changes, which is unique advantage compared with other methods. In particular, an uncertainty model is precisely established via a frequency-domain analysis approach to introduce the nonlinear characteristics and the statistical properties of identification into the H∞ control problem, which maintains the robustness of closed-loop WPT system. Finally, an experiment is given to verify the effectiveness of HMI method and proposed H∞ robust controller.**

***Index Terms*—H∞ robust controller, Hammerstein model-based identification (HMI) method, system identification, wireless power transfer (WPT).**

I. Introduction

WIRELESS power transfer (WPT) technology is widely applied in underwater equipment, electric vehicles (EV), industrial robots [1], [2], [3], [4], etc., owing to less physical contacts and remarkable characteristics, such as reliability, position free, and robustness. Modeling and control of magnetic resonance coupling WPT have been intensively studied since 2007, when researchers from MIT used strongly coupled magnetic resonance theory to achieve 60 W of transmitted power at a distance of 2 m [5].

For the applications of the WPT, such as wireless EV chargers, the component parameters are usually unknown and difficult to precisely measure due to coils misalignment, load variations, and device aging [6], [7], [8], [9]. Consequently, obtaining the precise WPT system model using analytical methods, such as d-q decomposition [10], before each run becomes highly difficult. Therefore, data-driven modeling methods have been introduced in WPT to achieve rapid system modeling [6], [11], [12], [13], [14]. Furthermore, phase-shift control has always been a research focus in the field of WPT due to its flexible control capabilities and ability to maintain the system in resonance. Various phase-shift methods have been proposed for different WPT topologies [15], [16], [17]. However, different phase-shift control strategies introduce varying nonlinear characteristics to the system. Unfortunately, the control method for nonlinear perturbations has not received sufficient attention in the existing literature. Therefore, it is essential to develop a data-driven approach that considers the system's nonlinearity to achieve rapid nonlinear modeling and control design for WPT systems. To address these challenges, this article introduces Hammerstein model-based identification (HMI) methodologies to the realm of WPT system modeling.

Data-driven modeling for the WPT system is still in its early stages of development. To establish a precise WPT system model directly from experimental data, a data-driven modeling method is proposed in [6]. This study employs analytical modeling methods to ascertain the model structure and system modeling techniques to determine model parameters, thereby accurately describing system behavior at a given steady-state point. However, the model's applicability to other working points and its effectiveness in closed-loop control have not been validated. In [12], a simplified data-driven modeling approach is developed to obtain an acceptable model with an approximate time delay for controller design purposes. The fit ratio of the identified model can reach up to 94%, which is sufficient to describe the dynamic model of the system. However, the focus remains on the specific steady-state point, and the method's effectiveness at other steady-state points has not been addressed. In [7], a recursive refined instrumental variable method is proposed to achieve data-driven modeling of WPT systems where the load may vary slowly over time. The inherent nonlinearity caused by load variations in WPT is represented by a state-dependent parameter nonlinear model. However, the control of the WPT system under load and steady-state point changes needs to be addressed in this article.

More recently, an excitation signal optimization method for data-driven modeling of the WPT systems has been proposed in [11], where the quality of parameter estimation is improved

Manuscript received 22 August 2023; revised 27 October 2023; accepted 3 December 2023. Date of publication 14 December 2023; date of current version 16 May 2024. This work was supported by the National Natural Science Foundation of China under Grants 51907054 and 51977151. Recommended for publication by Associate Editor A. Kuperman. *(Corresponding authors: Qijun Deng; Zhifan Li.)*

Shuaiqi Li, Qijun Deng, Zhifan Li, Chang Yu, Kaicong Cui, and Peng Luo are with the School of Electrical Engineering and Automation, Wuhan University, Wuhan 430072, China (e-mail: lishuaiqi@whu.edu.cn; dqj@whu.edu.cn; lizhifan@whu.edu.cn; yuchang@wust.edu.cn; kaicong.cui@whu.edu.cn; luo.peng@whu.edu.cn).

Jiangtao Liu is with the School of Physical, Mechanical and Electrical Engineering, Hubei University of Education, Wuhan 430205, China (e-mail: liujiangtao@whu.edu.cn).

Color versions of one or more figures in this article are available at https://doi.org/10.1109/TPEL.2023.3343085.

Digital Object Identifier 10.1109/TPEL.2023.3343085

using the receding horizon D-optimization method. However, none of the abovementioned methods have taken into account the nonlinearity introduced by different phase-shift control methods. As a result, the designed controllers can only guarantee effectiveness near the given steady-state point.

Phase-shift control has always been a research focus in the field of WPT, and various phase-shift methods have been proposed for different topologies. A dual-side phase-shift control of the strongly coupled series-series compensated WPT systems is proposed in [16]. The phase shift method proposed in [16] regulates the output current by changing the phase difference between the primary-side and the secondary-side converters. However, the nonlinearity introduced by the phase shift method on the control performance has not been addressed. In [17], two phase-shift control strategies are proposed for a two-phase dual-frequency system with two loads. The open-loop system's output power is analyzed under both phase-shift control methods. In addition, a closed-loop control scheme based on the phase-shift control approach is designed to achieve stable output power precisely and prevent load imbalances. However, the inherent nonlinearity of the phase-shift control method and its impact on the closed-loop system's disturbances are not discussed in this article. In [12], a control strategy known as the optimal zero voltage switching (ZVS) modulation strategy has been investigated. This method offers a wider controllable phase range for maintaining ZVS compared with traditional phase-shift control methods. However, the impact of the proposed phase shift method on control as well as identification has not been thoroughly studied.

In addition, diverse control techniques, including PID control [18], internal model control (IMC) [12], and robust control [8], [19], [20], [21], have been explored for regulating the WPT system. A standard H∞ robust controller for *CLC* magnetic resonance coupling WPT system is explored in [19]. However, the weighted function of H∞ robust controller is calculated only based on the frequency domain characteristics of the external disturbance and the variation of the model parameters, without considering the nonlinear disturbance of the system itself. The robust controllers proposed in [8], [20], and [21] guarantee the performance of the nominal WPT system. But this method generally demands for knowledge of parametric perturbation and external disturbance, which is difficult to acquire in the field. The IMC method is developed in [12], assuring the stability of output voltage under the time delays. Nevertheless, the IMC method requires the acquisition of system model parameters and concrete time delays. The PID controller utilized in [18] is tuned using the Ziegler–Nichols tuning method, resulting in a satisfactory transient response for the bidirectional WPT system with multiple pickups. But this approach cannot achieve the ideal control performance when the model changes.

In brief, the design of a superior controller generally requires accurate system modeling, which depends on the knowledge of exact circuit component parameters. But the parameter values would drift from the nominal ones under the aging of device. It is difficult to obtain all of the component parameters in practical scenarios to construct the model. Notably, in those existing approaches, control and identification are irrelevant processes with different optimization objectives. It is fascinating to utilize the information from the identification to design robust controllers.

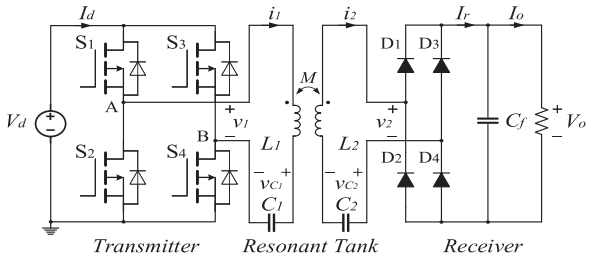

Fig. 1. Circuit topology for WPT system under consideration.

The Hammerstein model allows the linear and nonlinear parts of the system to be represented separately, which helps to obtain an accurate model of the system over the entire range of operations. This article aims to investigate the utilization of the HMI technique in the WPT systems to address the adverse effects of inherent system nonlinearities and estimation errors on control performance. In order to achieve robustness in the closed-loop system when the working point changes, it is imperative to incorporate the nonlinear characteristics of the WPT system into the controller design process. Achieving robustness in the closed-loop system against variations in working points requires incorporating the nonlinear characteristics of the WPT system into the controller design process. Notably, the existing literature in the field of WPT lacks attention to this crucial aspect. Compared with other existing control-oriented modeling methods, the major contributions of this article can be summarized as follows.

1) To ensure the control performance of the WPT system under inherent nonlinearities as well as system modeling error perturbations, an improved H∞ robust controller is introduced based on the proposed uncertain model.
2) A new method is proposed for the establishment of an uncertainty model in the field of the WPT H∞ control, which implicitly takes the nonlinearities of inverter, resonance tank, and rectifier into account.
3) To obtain dynamic as well as static characteristics of the WPT system over the entire operating range without incurring additional costs, a simplified WPT identification and controller design method is proposed.

The rest of this article is organized as follows. A detailed mathematical model and system identifiability analysis are presented in Section II. The HMI method of the WPT system is introduced in Section III. An uncertainty model and the H∞ robust controller is established in Section IV, followed by the experiment of the proposed controller under disturbances in Section V. Finally, Section VI concludes this article.

II. Model Equivalent of the WPT System

A classical series–series compensated WPT system shown in Fig. 1 is considered for analysis, where V_d and I_d are the voltage and current of the inverter dc source, v_{C_1} and v_{C_2} are the voltages of capacitors C_1 and C_2, v_1 and v_2 are the input and

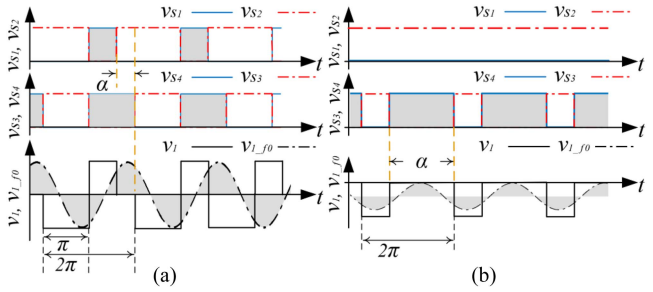

Fig. 2. Waveforms of the control signal in Fig. 1. $v_{s1} - v_{s4}$ are normalized control signals for switches $S_1 - S_4$, respectively. v_1 and v_{1_f0} are the input voltage and fundamental component of v_1, respectively. (a) Control angle α in the range of [0–π). (b) Control angle α in the range of [π–2π].

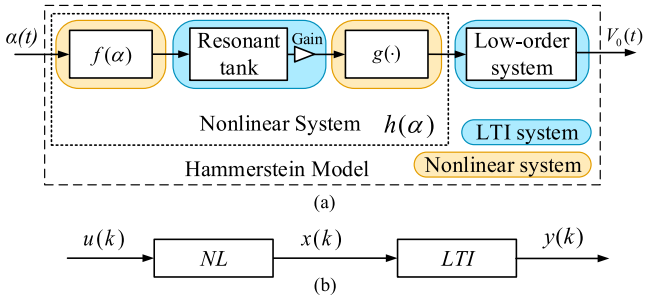

Fig. 3. Structure of the system. (a) WPT system. (b) Equivalent Hammerstein model.

output voltages of the resonant tank, i_1 and i_2 are the input and output currents of the resonant tank, I_r is the root mean square value of the rectifier bridge output current, and I_o and V_o are the load voltage and current, respectively.

The basic fundamentals of WPT system researched in this article are as follows:

$$L_1\frac{di_1}{dt} = v_1 - v_{C_1} + M\frac{di_2}{dt} - i_1R_1 \tag{1}$$

$$L_2\frac{di_2}{dt} = M\frac{di_1}{dt} - v_{C_2} - v_2 - i_2R_2 \tag{2}$$

$$C_1\frac{dv_{C_1}}{dt} = i_1 \tag{3}$$

$$C_2\frac{dv_{C_2}}{dt} = i_2 \tag{4}$$

$$C_f\frac{dV_o}{dt} = I_r - \frac{V_o}{R_o}. \tag{5}$$

The full-bridge inverter is adopted in this article, and its circuit diagram is shown in gray in Fig. 1. The output voltage and resulting charging power of the inverter can be regulated by adjusting the control angle α. To obtain a larger range of adjustable control angles and ZVS soft-switching phase margins, a control strategy known as optimal ZVS is applied in this article [12], and the optimal ZVS-based α adjustment waveforms are shown in Fig. 2, where $v_{s1} - v_{s4}$ represent the control signals for switches S_1 to S_4, respectively, while v_1 and i_1 denote the input voltage and current of subsystem 2, respectively. Consider [0 1] as the normalized adjustment range of α, where α originally ranges from 0 to 2π. The system exhibits a strong nonlinearity when α is tuned around 0.5, which brings new challenges to the control of the WPT system.

For the WPT system shown in Fig. 1, the following assumptions are made.

Assumption 1:

1) The switches and diodes are ideal components.
2) The switching frequency is fixed.
3) Both the sending and receiving resonators are at or sufficiently close to the resonant state.

Remark 1: Assumption 1) simplifies the model by neglecting power loss, while Assumption 2) ensures fixed frequency components of v_1 and v_2 in the frequency domain when determining the control angle. Assumption 3) allows only the first harmonic to pass through the resonant tank, guaranteeing the accuracy of the first harmonic approximation.

In this section, we investigate the model equivalence of the system by analyzing the primary physical mechanisms of the various modules within the WPT system. The aim is to simplify the system analysis by decomposing the complex WPT system into four distinct subsystems. The validity of this approach is demonstrated by analyzing the static and dynamic characteristics of each subsystem. Fig. 3(a) illustrates the four subsystems that comprise a WPT system.

1) Subsystem 1: Subsystem 1 converts α to the inverter high-frequency ac output voltage v_1 when a dc source voltage of V_d is supplied. The principle of the optimal ZVS-based α adjustment strategy can be expressed in terms of (6):

$$\begin{aligned} v_1 &= \hat{V}\sin(\omega_s t + \varphi_u) \\ \hat{V} &= V_d\sqrt{a^2+b^2}/(\pi) \\ \varphi_u &= \arctan(a/b) \\ a &= -\cos(\alpha), \quad b = 3+\cos(\alpha) \end{aligned} \tag{6}$$

where ω_s is the switching frequency calculated as $\omega_s = 2\pi f_0$ and f_0 represents the switching frequency of the converter. Furthermore, the voltage v_1 is expressed as the sum of voltages at points A and B in Fig. 1, i.e., $v_1 = v_a + v_b$.

The equations presented in (6) illustrate that subsystem 1 is memoryless and responds swiftly to alterations in input α without affecting the system's low-frequency behavior. Hence, the characteristics of subsystem 1 can be effectively captured by a nonlinear block denoted as $f(\alpha)$.

2) Subsystem 2: Subsystem 2 denotes the transformational relation of the input transmitter voltage v_1 to the receiver resonant current i_2 in the resonant tank. The classical series–series compensated resonance circuit is shown in blue in Fig. 3(a). Based on Kirchhoff's voltage law, the following equations are obtained:

$$v_1 = i_1R_1 + v_{C_1} + L_1\frac{di_1}{dt} - M\frac{di_2}{dt}$$

$$i_1 = C_1\frac{dv_{C_1}}{dt}$$

$$M\frac{di_1}{dt} = L_2\frac{di_2}{dt} + v_2 + i_2R_2 + v_{C_2}$$
$$i_2 = C_2\frac{dv_{C_2}}{dt}. \tag{7}$$

3) Subsystem 3: Subsystem 3 pertains to the nonlinear transformation of the ac signal i_2 to a dc signal I_r, which is accomplished via the rectifier bridge illustrated in the yellow segment of Fig. 3(a). Mathematically, this process is represented as

$$I_{\mathrm{r}} = \sqrt{\frac{1}{T_r}\int_{t-T_r}^{t} i_2^2\, dt} \tag{8}$$

where $T_r = 2\pi/\omega_s$. When the switching frequency ω_s is constant, the conversion of i_2 to I_r can be represented by a nonlinear term $I_r = g(i_2)$, where i_2 is the input signal.

4) Subsystem 4: Subsystem 4 can be represented by an RC parallel filter circuit to eliminate ripples and spikes at each frequency of the output load voltage V_o. The RC circuit filters I_r to generate the output load voltage V_o, which is represented the low-frequency behavior of the system

$$V_o = \frac{1/C_f}{p + 1/(RC_f)} I_r. \tag{9}$$

In order to achieve a smooth output voltage, the value of the filter capacitor C_f is chosen to be very large. Specifically, the RC filter circuit serves as the only significant source of low-frequency response in the system.

Notably, it can be seen from (6) that when the system parameters are determined, the nonlinear subsystem $f(\alpha)$ is only a function of the α. The static gain K of linear subsystem 2 exhibits constancy under the condition of an unchanged input spectrum of subsystem 1. Subsystem 3 is independent of the system parameters, which is considered as the inherent nonlinear term of the WPT system. To facilitate analysis and simplify the model structure, the series subsystems 1–3 are combined into an equivalent nonlinear system $h(\alpha)$. So that the WPT system can be described by a nonlinear model of Hammerstein type and represented by

$$V_o = G(z)h(\alpha) \tag{10}$$

where $G(z)$ denotes the discrete-time transfer function of the linear time-invariant (LTI) model, and z is the difference operator. In this article, the bilinear transformation is used to transfer the model from continuous-time forms to discrete-time forms based on z-transform. The sampling time $T_s = 1$ ms is selected with considering of hardware limitation and bandwidth requirement.

Fig. 3(b) shows a standard discrete Hammerstein model, where $u(k)$ denotes $u(kT_s), k \in \mathbb{N}^+$, is input variable (i.e., the control angle α), $NL = h(\alpha)$ denotes the nonlinear static characteristic, $x(k)$ indicates I_r and $y(k)$ represents the output voltage V_o. LTI denotes the linear part of WPT, which will be explained in detail in Section III.

In this article, we suppose that the actual parameters of circuit components are fixed when the system starts to work. The main component parameters are listed in Table I. According to (8) and (9), the variation of α will not change the structure or parameters of the nonlinear model for subsystems 1 and 3.

TABLE I
PARAMETRIC VALUES OF THE WPT SYSTEM

Parameter	Explanation	Value
f_s	Switching Frequency	92 kHz
V_d	DC Voltage	300 V
L_1	Self-inductance of Primary coil	110 μH
L_2	Self-inductance of Secondary coil	110 μH
C_1	Primary resonant capacitance	26 nF
C_2	Secondary resonant capacitance	25.4 nF
M	Mutual inductance	41 μH
C_f	Filter capacitance	600 μF
R_L	Load resistance	35 Ω
T_s	Sampling time	1 ms

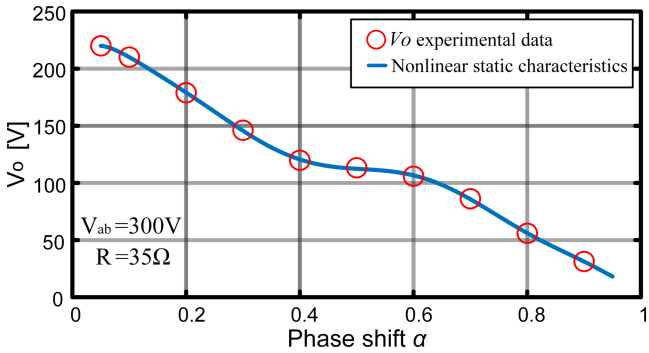

Fig. 4. Nonlinear static characteristics of the WPT system.

Besides, neglecting the influence of C_f, with v_1 as the input and i_2 as the output, the differential equations shown in (7) are converted to a transfer function form as follows:

$$G_{\mathrm{resonance}} = \frac{C_1\, s^3}{\beta_1\, s^4 + \beta_2\, s^3 + \beta_3\, s^2 + \beta_4 s + \beta_5} \tag{11}$$

where s is the Laplace operator, $\beta_1 = -C_1\frac{M^2 - L_1L_2}{M}$, $\beta_2 = \frac{C_1(L_1(R_0+R_2)+L_2R_1)}{M}$, $\beta_3 = \frac{C_2L_2+C_1L_1+C_1C_2R_1(R_0+R_2)}{C_2\, M}$, $\beta_4 = \frac{(R_0+R_2)C_2+C_1R_1}{MC_2}$, and $\beta_5 = \frac{1}{C_2\, M}$.

For an actual WPT system with optimal ZVS phase-shift control technique, the output voltage V_o is regulated by adjusting α while keeping the switching frequency $w_s = 2\pi f_s$. Therefore, the effect of the resonant tank (i.e., subsystem 2) can be considered as a static gain K under the steady state [13]. Additionally, the nonlinear model $h(\alpha)$ can be expressed using (6) and (8).

$$h(\alpha) = f(\alpha) \cdot K \cdot g(\cdot). \tag{12}$$

III. CONTROL-ORIENTED MODELING

A. Identification of WPT Nonlinear Static Characteristics

An open-loop experiment with the circuit shown in Fig. 1 is performed to determine the nonlinear static characteristics of the WPT system. First, a pulse signal of α is provided to vary from 0 to 1 at intervals of 0.1 and figured as $\alpha_i = [0.1, 0.2, \ldots, 0.9], (i = 1, 2, \ldots, 9)$. Then, for each value of α_i, the steady-state voltage Vo_i is measured and recorded with an oscilloscope, and the experimental measurement points are shown as red circles in Fig. 4. After that, the measured voltage Vo_i sequence is fitted to the α_i sequence using a sixth-order

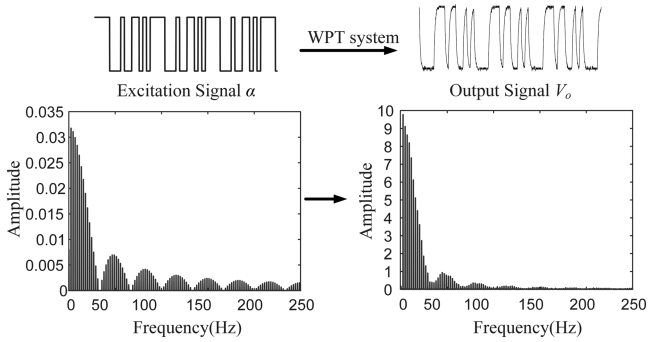

Fig. 5. Waveform and spectrum of the system's excitation signal and the output signal V_o.

polynomial. Finally, the nonlinear characteristic is represented by the continuous line in Fig. 4.

B. Identification of LTI Part of WPT

To improve identification accuracy, the fourth-order PRBS sequence is selected by using the method proposed in [11], which is generated by a four-stage shift register and determined by three parameters, amplitude A, λ, and interval T_s. The amplitude A is chosen switching between ± 0.02 at each working point and the value of clock period $\lambda = 30T_s$, where $T_s = 1$ ms as listed in Table I. The PRBS signal predominantly excites the mid- to low-frequency characteristics of the system, which also represent the dominant mode of the WPT system. Fig. 5 illustrates the waveforms and spectra of the system's excitation signal and the output signal V_o. It can be observed that the high-frequency components in the PRBS excitation signal are filtered out. This observation suggests that, under the current conditions, the WPT system can be reasonably approximated as a low-order system.

The stochastic recursive least squares (SRLS) method [22] is employed in this article to obtain the model of the WPT system. This technique offers the advantage of simultaneously estimating the covariance of the model parameters, which can assist in designing a robust controller. The LTI part of WPT (i.e., $G(z)$) is considered as the autoregressive model with exogenous inputs (ARX) form, which is assumed to have the following linear regression form:

$$A(z^{-1})y(k) = B(z^{-1})u(k) + e(k) \tag{13}$$

where the measurement $y(k)$ of output voltage is assumed to be contaminated by Gauss white noise $e(k)$, $A(z^{-1})$ and $B(z^{-1})$ are numerator and denominator polynomials of the transfer function of $G(z)$. The equation can be written in form of linear systems of equations

$$\mathbf{z}(k) = \mathbf{h}^T(k)\mathbf{\Theta} + \mathbf{e}(k) \tag{14}$$

where superscript T denotes the vector/matrix transpose, n_a and n_b represent polynomial degrees, $\mathbf{h}^T(k) = [-y(k-1), \ldots, -y(k-n_a) - u(k-1), \ldots, -u(k-n_b)]$ is the data vector, and $\mathbf{\Theta} = [a_1, a_2, \ldots, a_{n_a}, b_1, b_2, \ldots, b_{n_b}]$ is the parameter vector, respectively. In particular, the assumptions about $e(k)$ are made.

Assumption 2:

1) $e(k)$ is a zero-mean sequence of random variables with a Gaussian amplitude distribution, which is independent of $\mathbf{h}^T(k)$ i.e., $E\{e(k)\} = 0$, $E\{\mathbf{h}^T(k)e(j)\} = 0 \quad \forall k, j$.
2) Serially uncorrelated and have a constant variance: i.e., $E\{e(k)e(j)\} = \sigma_e^2\delta_{kj}$ where δ_{kj} is the Kronecker delta function.

The SRLS technique is utilized in this article for the purpose of estimating linear systems. The SRLS algorithm offers the advantage of obtaining parameter estimates and error covariance matrix $\mathbf{P}^{(k)}$ at every sampling instant, providing a convenient way to quantify the modeling uncertainty of the identified model for robust controller design [22].

From Assumption 2, it is known that e has a Gaussian amplitude distribution, and then it can be obtained that the parameter estimates $\hat{\mathbf{\Theta}}(k)$ and estimation errors $\tilde{\mathbf{\Theta}}(k)$ also have a Gaussian normal distribution of the form [23]

$$\hat{\mathbf{\Theta}}(k) = \mathcal{N}\left[\mathbf{\Theta}_0, \mathbf{P}^*(k)\right]; \quad \tilde{\mathbf{\Theta}}(k) = \mathcal{N}\left[\mathbf{0}, \mathbf{P}^*(k)\right]. \tag{15}$$

Notice that the statistical characteristics of the parameter estimates are completely determined by two statistical moments, namely, the true value of $\mathbf{\Theta}_0$, and the error covariance matrix $\mathbf{P}^*(k)$. Therefore, the standard error (SE) of estimated parameters can be obtained from $\mathbf{P}^*(k)$.

To design a controller, the low-frequency dynamics of a S-S WPT system are required, which is sufficient to be described by a first-order model [12]

$$G(z) = \frac{b}{z + a} \tag{16}$$

where a and b are the estimated parameters, and z is the discrete time operator with a discrete time of T_s. The WPT system with parameters listed in Table I is excited by the input sequence designed in Section II and yields data for identification. Afterward, the experimental data sequences of $[h(\alpha)(k), V_o(k)]$ is uploaded to the PC for identification. Finally, the LTI model $G(z)$ is obtained by using the SRLS algorithm on MATLAB.

Since the data collected at $\alpha = 0.2$ have a high signal-to-noise ratio and are less affected by nonlinearity, take the working point $\alpha = 0.2$ as an example, 1500 sets of input–output data are collected with a sampling time of 1 ms. The LTI model $G_2(z)$ is obtained by applying the above method. By applying (10), the nonlinear model of the WPT system is expressed as $h(\alpha)G_2(z)$. The recursive stochastic estimation results (i.e., blue line) obtained using SRLS method and the varying residual estimates (i.e., gray area) are shown in Fig. 6. Here, the estimates of the two parameters and the SE bounds are shown in the two plots. $\mathbf{P}^*(k)$ is directly interpreted as the prior covariance matrix in the SRLS algorithm [23], and is utilized to calculate the SE bounds within certain definable confidence bounds. SE bounds are used to provide bounds on the uncertainty of the estimated system model, which evaluates the quality of the model. To ensure the accuracy, the confidence interval of estimated parameters with

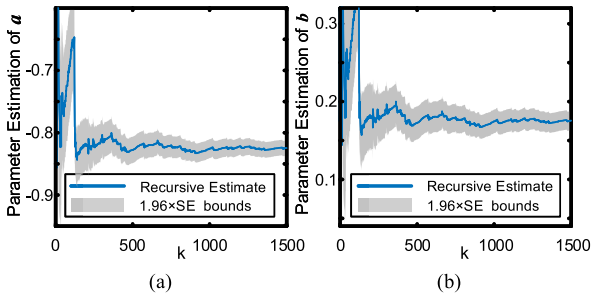

Fig. 6. Recursive parameter estimates and their estimated SE bounds of G_2. (a) Parameter estimation of a. (b) Parameter estimation of b.

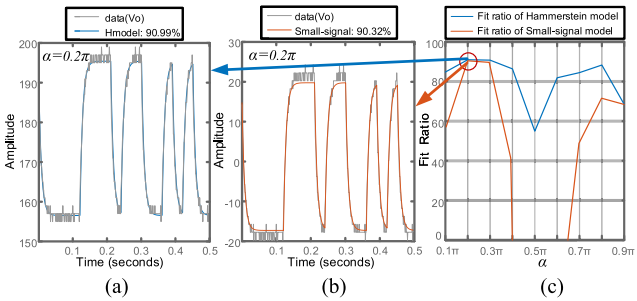

Fig. 7. Fit ratios of the Hammerstein model and the analytical model. (a) Comparison between the Hammerstein model output and measured output as α is varied around 0.2. (b) Comparison between the analytical small-signal model output and measured output as α is varied around 0.2. (c) Fit ratio of Hammerstein model and analytical small-signal model at all working points.

TABLE II
DISCRETE TRANSFER FUNCTIONS OF THE ARX MODEL

Phase-Shift α	$G_i(z)$	Phase-Shift α	$G_i(z)$
[0.08 0.12]	$G_1 = \frac{0.4416}{z-0.5582}$	[0.58 0.62]	$G_6 = \frac{0.449}{z-0.5478}$
[0.18 0.22]	$G_2 = \frac{0.4565}{z-0.5409}$	[0.68 0.72]	$G_7 = \frac{0.4453}{z-0.5528}$
[0.28 0.32]	$G_3 = \frac{0.4562}{z-0.5408}$	[0.78 0.82]	$G_8 = \frac{0.435}{z-0.5654}$
[0.38 0.42]	$G_4 = \frac{0.4551}{z-0.5418}$	[0.88 0.92]	$G_9 = \frac{0.4013}{z-0.6077}$
[0.48 0.52]	$G_5 = \frac{0.4524}{z-0.544}$		

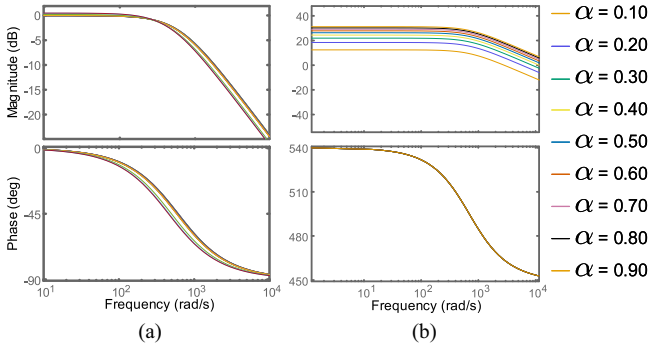

Fig. 8. Bode diagrams of the model as α vary. (a) Bode diagrams of the nine identified ARX models based on the HMI method. (b) Bode diagrams of nine small-signal models using the analytical approach.

a 95% confidence level is constructed in this article. The upper and lower bounds of the 95 % confidence level are calculated as follows:

$$\text{Upper Bound} = \boldsymbol{\Theta}(k) + (\text{SE} \times 1.96) \tag{17}$$

$$\text{Lower Bound} = \boldsymbol{\Theta}(k) - (\text{SE} \times 1.96) \tag{18}$$

where $\boldsymbol{\Theta}(k)$ is the estimates of a and b at k, SE is computed as the square root of the diagonal elements of the $\mathbf{P}^*(k)$ matrix, and 1.96 is the approximate value of the 95% percentile point of the normal distribution.

The fit ratio is a common metric to assess the accuracy of an identified model, measuring the similarity between its predicted output and the actual measurement. Using the MATLAB command "compare," the corresponding time domain comparison curve of the predictive model output and the measured output can be obtained. For comparison, the small-signal models $Ga_2(z)$ is established by analytical method at $\alpha = 0.2$. Fig. 7(a) and (b) illustrate the differences between the measured data and model response of the Hammerstein model and analytical model, respectively. The percentages shown in the legends are the fit ratios, and the fit ratios of the Hammerstein model and analytical model are 90.99% and 90.32%. Small differences between the model and experimental results are considered as random noise. The high fit ratios show that both the Hammerstein model and the analytical small-signal model established at the $\alpha = 0.2$ can well describe the dynamic characteristics of the system.

In order to validate the accuracy of the models with varying α, the measured output of the WPT system is compared with the outputs of the Hammerstein and analytical models at working points of $\alpha = 0.1, 0.2, \ldots, 0.9$, as shown in Fig. 7(c). The fit ratio curves of the Hammerstein model and analytical model are represented by the blue and red lines, respectively. The results indicate that the accuracy of the analytical model decreases rapidly as α changes, while the Hammerstein model maintains a high level of accuracy. Notably, the degree of matching for the analytical model is extremely low, resulting in fit ratios of 0 for Ga_2 at $\alpha = 0.5, 0.6$.

To characterize the WPT system for α over its full operating range [0 1], this range is divided into nine subintervals (see Table II).

In Table II, $G_i(z), i = 1, 2 \ldots 9$ are identified by SRLS method using data sequences of $[h(\alpha)(k), V_o(k)]$ for each small intervals of α. For comparison, the small-signal models $Ga_i(z), i = 1, 2 \ldots 9$ are established by analytical method at same working points [10]. The bode diagrams of G_i and Ga_i are shown in Fig. 8(a) and (b), respectively. Due to the gain of α to V_o is embedded in a nonlinear static mapping (see Fig. 4), the static gain of G_i is almost equal to 0 dB, while the static gain of Ga_i is varies from 6 to 31 dB. In other words, G_i is independent of α, while the gain of Ga_i depends largely on the α. Notice that, G_i and Ga_i exhibit similar dynamic characteristics in frequency range of 500–1000 rd/s, which indirectly confirms the accuracy of the HMI method.

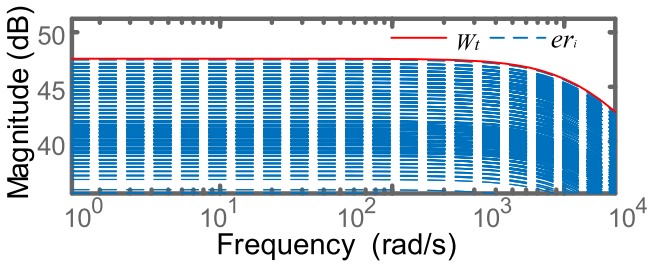

Fig. 9. Bode-magnitude diagram of W_t and er_i.

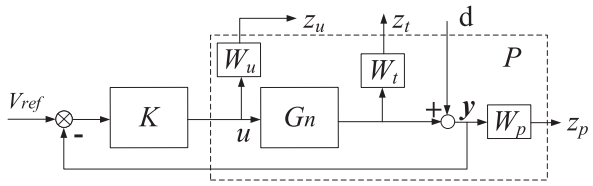

Fig. 10. Structure diagram of H∞ problem for the WPT system.

IV. Design of Robust Controller

This article aims to develop a controller that can maintain satisfactory control performance for the WPT system with significant nonlinearity, instead of designing an optimal control for a specific working point.

A. Uncertainty Analysis of WPT System

In order to take the HMI method into the H∞ problem of WPT, the identified model is considered as the nominal model G_n, and the actual system is described by multiplicative uncertainty

$$G_s = G_n\,(1 + \Delta W_t) \tag{19}$$

where Δ represents the normalized uncertainty that satisfies $\|\Delta\|_\infty \le 1$, and W_t is the weighted function, which contains the uncertainty of the system. The highest fit ratio of G_2 implies a better description of the system dynamics. Therefore, G_n is chosen to be equal to G_2. The nonlinear characteristics of the WPT caused by converter and rectifier have been discussed in detail in Section IV, where the system gain varies nonlinearly from 220 to 0 as α varies between 0 and 1. Under Assumption 2, the parametric uncertainty of the WPT system is acquired by the UpperBound and LowerBound of the estimates. With the consideration of parameter perturbation range and calculation accuracy requirements, 7 points are sampled equally between the upper and lower bounds of the a and b parameters, represented by $[a_{r1}, a_{r2}, \ldots, a_{r7}]$ and $[b_{r1}, b_{r2}, \ldots, b_{r7}]$, respectively. Therefore, there are $7 \times 7 = 49$ possible transfer function combinations. After superimposing nonlinear gains, the corresponding transfer function can be expressed as: $G_{si}(i = 1, 2, \ldots, 49)$. Based on the parameter perturbations and the nonlinear static gain, the magnitude error e_{ri} between the nominal system and the specific system G_{si} can be figured out as

$$|W_t(j\omega)| \ge |\Delta W_t(j\omega)| \ge er_i = \left|\frac{G_{si}(j\omega) - G_n(j\omega)}{G_n(j\omega)}\right| \tag{20}$$

where Δ represents the normalized uncertainty that satisfies $\|\Delta\|_\infty \le 1$ and W_t is the weighted function containing information on the frequency characteristics of the uncertain nonlinear gain and parameter estimation error. In order to obtain an accurate uncertainty model to describe the dynamic performance of the system under perturbation, a frequency domain analysis method is introduced. Fig. 9 shows the amplitude–frequency characteristics of the system under the disturbance of statistical properties of the SRLS approach and the nonlinearity of WPT. The disturbance has a significant effect on the frequency characteristics, especially in the low and medium frequency range in terms of amplitude. It is necessary to concentrate the weighting function W_t on the frequency range below 10 k rad/s, which is closely related to the controller performance. The weighting function W_t is chosen to be a second-order system with the consideration of the balance between controller performance and controller computability. Finally, W_t is calculated by the linear fitting tool in the MATLAB math box as follows:

$$W_t = \frac{0.0001836z - 0.0001642}{z^2 - 1.877z + 0.8765}. \tag{21}$$

B. H∞ Controller Design

When $h(\alpha)$ is obtained and strictly monotone, the structure diagram of the H∞ problem for the WPT system can be depicted with Fig. 10. Then, the generalized plant P with uncertainty is obtained, where d is the external disturbance, V_{ref} is the reference input, y and u are the output and input of the WPT system, K is the H∞ controller, W_p and W_u are the weighting functions and $z = [z_p \quad z_u \quad z_t]^T$ is the constructed evaluation function of H∞ controller, as detailed in [8] and [20]. Based on the previous uncertainty analysis, the robust stability of the WPT system transformed into a standard H∞ optimal problem based on small gain theory. In order to achieve a strong anti-interference capability and a smaller steady-state error of the closed-loop system, the weighting functions W_p and W_u are selected as follows by using the approach proposed in [8]:

$$W_p = \frac{1500}{s+1}; W_u = 500\,000. \tag{22}$$

In order to ensure the system control performance and reduce the order of the closed-loop system, the reduced-order controller is designed as

$$K = \frac{1.31e5\ s^3 - 7.39e6\ s^2 + 2.44e14s + 5.97e16}{s^4 + 2.35e4\ s^3 + 2.69e9\ s^2 + 3.65e13s + 3.64e13}. \tag{23}$$

V. Experimental Verification

The experimental prototype, illustrated in Fig. 11, comprises a full-bridge inverter with four 1200 V SiC Trench MOSFETs (IMW120R045M1), supplied by a dc source (REG75030). The inverter generates high-frequency input voltage to the resonant tank, containing two shunt capacitors and two transmission coils with 9 turns of Litz wire. The shunt capacitor consists of several 1 nF capacitors (EPCOS), and the transmission coils are made by winding 9 turns of Litz wire. To reduce the inductive resistance

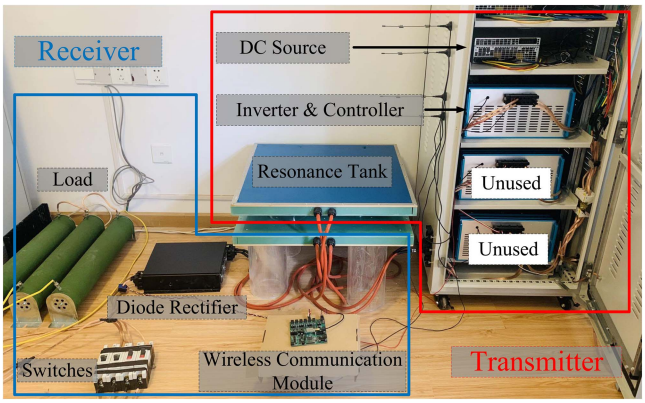

Fig. 11. Circuit topology for ICPT system under consideration.

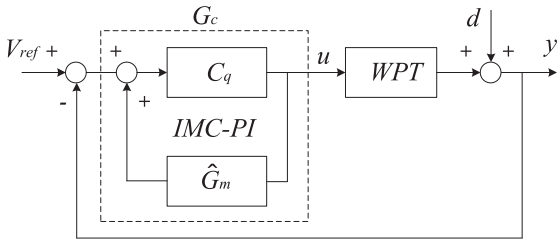

Fig. 12. Equivalent IMC structure.

and improve the quality factor of the coils, the number of strands in the stranded bundle is chosen to be 3000. Finally, the Schottky diodes (IDW40G120C5B) are used in the ac/dc rectifier to generate dc voltage output. The voltage is measured and displaced by an oscilloscope (TektronixMSO2024B). Furthermore, the proposed H∞ robust controller has been implemented on the ARM (STM322F407VGT), and an FPGA (XC6SLX9-3TQG1441) is used to generate the precise control signals. The high-speed communication between them is performed by CAN protocol. To verify the effectiveness of the control method proposed in this article, a PI controller based on the IMC method at the working point $\alpha = 0.2$ is designed simultaneously as a comparison [12].

The control block diagram of the IMC-PI controller is shown in Fig. 12, where C_q represents the IMC controller, G_c is the equivalent unit feedback IMC-PI controller, WPT represents the WPT system, and $\hat{G}_m$ is the estimation of the WPT system. Based on the design method presented in [12], the discrete IMC-PI controller is derived as

$$G_c = \frac{-0.004033z + 0.001733}{z - 1}. \tag{24}$$

Figs. 13(a) and 14(a) indicate that both IMC-PI and H∞ robust controller exhibit similar performance when the WPT system operates around $\alpha = 0.2$. Both controllers have zero steady-state error and neither has overshooting. The load resistor receives a power of 1.36 kW, with a measured dc–dc power efficiency of 92%. According to [24] and [25], the total power losses of all components are approximately 83 W, accounting for 6% of the total input dc power. Considering magnetic core losses and measurement errors, the measured efficiency value is reasonable.

TABLE III
CONTROL PERFORMANCE OF THE IMC-PI AND THE H∞ ROBUST CONTROLLER

	IMC-PI Controller		H∞ Robust Controller	
Variation of voltage [V]	100 to 130	30 to 130	100 to 130	30 to 130
Overshoot	/	/	/	/
Setting time [ms]	**50**	100	**50**	60
Setting time Variation Rate	**Initial value**	100%	**Initial value**	20%
Setting time [ms] under M change	80	120	50	60
Setting time Variation Rate	60%	140%	0	20%

Around the working point where $\alpha = 0.2$, both the IMC-PI controller and H∞ robust controller have a setting time of about 50 ms when the reference voltage increases from 100 to 130 V. However, under nonlinear system disturbances, the H∞ robust controllers demonstrate superior performance compared with the IMC-PI controllers. This can be observed in Fig. 13(b), where the IMC-PI controller's voltage waveform shows a distinct "staircase" when the adjustment range of α passes through the nonlinear region (around $\alpha = 0.5$), leading to a longer setting time of approximately 100 ms. In contrast, as shown in Fig. 14(b), the H∞ robust controller consistently exhibits strong performance with only minor variations in its setting time (approximately 60 ms). Comparing Figs. 14(c) and 13(c), it can be observed that in the voltage reduction experiment, the H∞ robust controller still demonstrates superior control performance.

As shown in Table III, when adjusting the voltage setpoint at the equilibrium point, there is minimal difference in the rise time and setting time between the H∞ and IMC-PI controllers (45 ms vs. 40 ms and 50 ms vs. 50 ms, respectively). However, when the system voltage is adjusted over a wide range, i.e., when the system operates away from the initial working point, the IMC-PI controller's setting time increases from 50 ms to 100 ms, representing a substantial increase of 100%. In contrast, the H∞ controller's setting time only experiences modest changes of 20%. Therefore, the authors believe that the experimental results fully demonstrate the superiority of the H∞ controller in the presence of nonlinear disturbances.

The "staircase" phenomenon is characterized by a prominent plateau in the waveform during the voltage rise phase, where the PI controller tends to accumulate integrals and exhibit large control volumes, leading to a degradation in control performance. This indirectly confirms the accuracy of the nonlinear characteristics mentioned in the Section II. The same experimental effect was observed for the voltage drop. The comparative evaluation of the control efficacy of two distinct controllers under the rise of reference voltage is depicted in Table III. The data presented in Table III clearly demonstrate that the H∞ robust controller performs significantly better than the IMC-PI controller in terms of both rise time and setting time variation rates.

When the mutual inductance value changes from 41 to 29 μH, the designed controller is still effective. This conclusion is

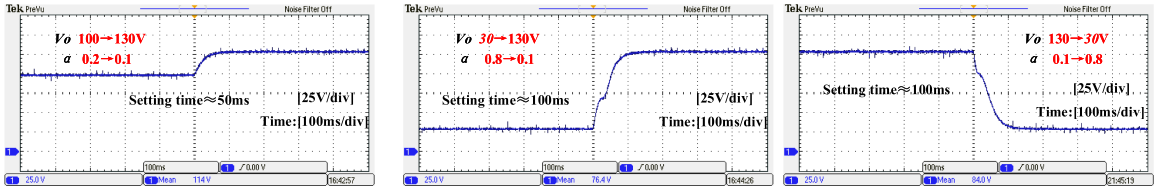

(a) (b) (c)

Fig. 13. Voltage variation control experiment of the IMC-PI controller designed at $\alpha = 0.2$. (a) V_o rises from 100 to 130 V. (b) V_o rises from 30 to 130 V. (c) V_o decreases from 130 to 30 V.

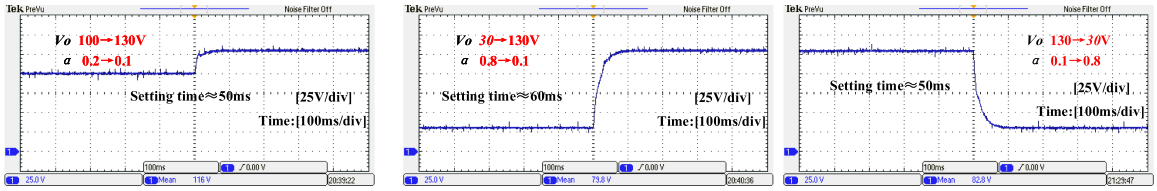

(a) (b) (c)

Fig. 14. Voltage variation control experiment of the proposed H∞ robust controller. (a) V_o rises from 100 to 130 V. (b) V_o rises from 30 to 130 V. (c) V_o decreases from 13 to 30 V.

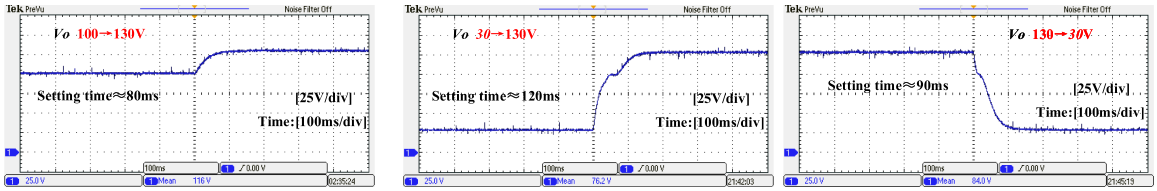

(a) (b) (c)

Fig. 15. Voltage variation control experiment with the IMC-PI controller at M = 29 μH. (a) V_o rises from 100 to 130 V. (b) V_o rises from 30 to 130 V. (c) V_o decreases from 130 to 30 V.

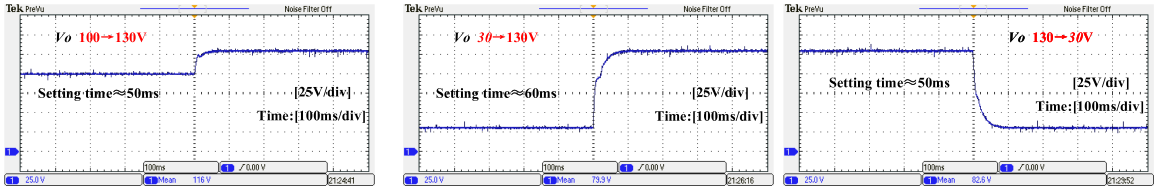

(a) (b) (c)

Fig. 16. Voltage variation control experiment with the proposed H ∞ robust controller at M = 29 μH. (a) V_o rises from 100 to 130 V. (b) V_o rises from 30 to 130 V. (c) V_o decreases from 130 to 30 V.

confirmed by the experimental results described in Figs. 15 and 16. When the mutual inductance changes, the H ∞ controller also exhibits a "staircase" phenomenon, but the setting time and rise time show little variation compared with when $M = 41$ μH. The IMC-PI controller exhibits similar control performance when $M = 41$ μH, and the control performance will deteriorates with the effect of the inherent system nonlinearity. It is worth noting that the system model underwent a transformation, and modifying the same voltage did not lead to an equivalent range of α variation.

Figs. 17 and 18 show the experimental waveforms of V_o for the load-switching moment and the distance-changing moment for the IMC-PI controller and H∞ robust controller, respectively. It can be observed that during load switching, the H∞ robust controller [see Fig. 18(a) and (b)] exhibits superior performance in terms of overshoot and setting time compared to the PI controller [see Fig. 17(a) and (b)]. In addition, the H∞ robust controller does not experience the "plateau" phenomenon (i.e., the voltage regulation stagnates briefly). Since the time for changing coil distance may not be consistent, comparing setting

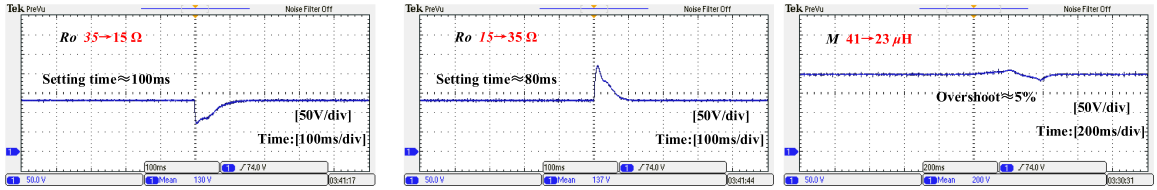

(a) (b) (c)

Fig. 17. Experimental waveforms of V_o in the load-switching moment and distance-changing moment under the IMC-PI controller. (a) Load resistance decreases. (b) Load resistance increases. (c) Distance-changing of coils.

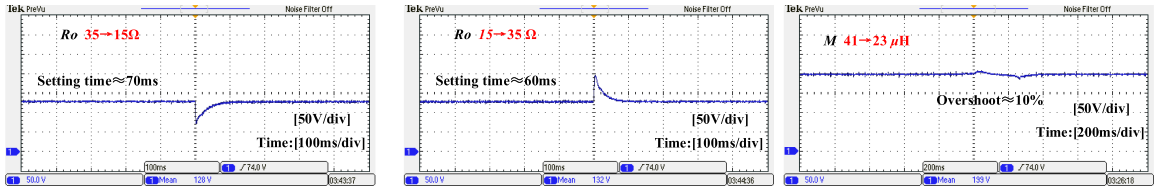

(a) (b) (c)

Fig. 18. Experimental waveforms of V_o in the load-switching moment and distance-changing moment under the proposed H∞ robust controller. (a) Load resistance decreases. (b) Load resistance increases. (c) Distance-changing of coils.

times may not be fair. However, from Figs. 17(c) and 18(c), it can be observed that the H∞ robust controller clearly exhibits a smaller overshoot compared with the IMC-PI controller.

VI. Conclusion

This article discusses the definition of the theoretical framework and experimental applications of the HMI method and identification-based H∞ robust control techniques in WPT systems. In particular, the nonlinearity and the modeling error cannot be ignored when designing the controller for a WPT system. To address this problem, a Hammerstein model of the WPT system is obtained. After that, a model set is established by the frequency domain analysis method based on the analysis of the statistical properties of the SRLS approach and the estimation of static nonlinear gain of the WPT system. Then, the standard structure of an H∞ control optimal problem is determined by using the small gain theory. Nonlinear perturbations and discriminative parameter errors are introduced into the controller design process based on the use of weighting functions, which improves the robustness of the system. The proposed H∞ robust controller has been experimentally verified on a prototype and further compared with the IMC-PI controller, and the results show the superiority of the method proposed in this article.

References

[1] H. Sekiya, K. Tokano, W. Zhu, Y. Komiyama, and K. Nguyen, "Design procedure of load-independent class-E WPT systems and its application in robot arm," *IEEE Trans. Ind. Electron.*, vol. 70, no. 10, pp. 10014–10023, Oct. 2023.

[2] Z. Zhang, H. Pang, A. Georgiadis, and C. Cecati, "Wireless power transfer–An overview," *IEEE Trans. Ind. Electron.*, vol. 66, no. 2, pp. 1044–1058, Feb. 2019.

[3] S. Li and C. C. Mi, "Wireless power transfer for electric vehicle applications," *IEEE Trans. Emerg. Sel. Topics Power Electron.*, vol. 3, no. 1, pp. 4–17, Mar. 2015.

[4] E. Rong, P. Sun, K. Qiao, X. Zhang, G. Yang, and X. Wu, "Six-plate and hybrid-dielectric capacitive coupler for underwater wireless power transfer," *IEEE Trans. Power Electron.*, vol. 39, no. 2, pp. 2867–2881, 2024.

[5] A. Kurs, A. Karalis, R. Moffatt, J. D. Joannopoulos, P. Fisher, and M. Soljačić, "Wireless power transfer via strongly coupled magnetic resonances," *Science*, vol. 317, no. 5834, pp. 83–86, 2007.

[6] F. Chen, H. Garnier, Q. Deng, M. K. Kazimierczuk, and X. Zhuan, "Control-oriented modeling of wireless power transfer systems with phase-shift control," *IEEE Trans. Power Electron.*, vol. 35, no. 2, pp. 2119–2134, Feb. 2020.

[7] F. Chen, A. Padilla, P. C. Young, and H. Garnier, "Data-driven modeling of wireless power transfer systems with slowly time-varying parameters," *IEEE Trans. Power Electron.*, vol. 35, no. 11, pp. 12442–12456, Nov. 2020.

[8] Y. Liang et al., "H∞ robust control for ICPT system with selected weighting function considering parameter perturbations," *IEEE Trans. Power Electron.*, vol. 37, no. 11, pp. 13914–13929, Nov. 2022.

[9] Z. Wei, B. Zhang, S. Lin, and C. Wang, "A self-oscillation WPT system with high misalignment tolerance," *IEEE Trans. Power Electron.*, vol. 39, no. 1, pp. 1870–1887, Jan. 2024.

[10] Q. Deng et al., "Modeling and control of inductive power transfer system supplied by multiphase phase-controlled inverter," *IEEE Trans. Power Electron.*, vol. 34, no. 9, pp. 9303–9315, Sep. 2019.

[11] Z. Li et al., "Receding horizon D-optimal input design for identification of wireless power transfer systems," *IEEE Trans. Emerg. Sel. Topics Power Electron.*, vol. 11, no. 3, pp. 3597–3606, Jun. 2023.

[12] Q. Deng, Z. Li, J. Liu, S. Li, P. Luo, and K. Cui, "Data-driven modeling and control considering time delays for WPT system," *IEEE Trans. Power Electron.*, vol. 37, no. 8, pp. 9923–9932, Aug. 2022.

[13] F. Chen, P. C. Young, H. Garnier, Q. Deng, and M. K. Kazimierczuk, "Data-driven modeling of wireless power transfer systems with multiple transmitters," *IEEE Trans. Power Electron.*, vol. 35, no. 11, pp. 11363–11379, Nov. 2020.

[14] J. Liu, G. Wang, G. Xu, J. Peng, and H. Jiang, "A parameter identification approach with primary-side measurement for DC–DC wireless-power-transfer converters with different resonant tank topologies," *IEEE Trans. Transport. Electrific.*, vol. 7, no. 3, pp. 1219–1235, Sep. 2021.

[15] X. Dai, J. Jiang, Y. Li, and T. Yang, "A phase-shifted control for wireless power transfer system by using dual excitation units," *Energies*, vol. 10, no. 7, 2017, Art. no. 1000.
[16] Y. Zhang, Z. Shen, Y. Wu, H. Wang, and W. Pan, "Dual-side phase-shift control for strongly coupled series–series compensated electric vehicle wireless charging systems," *World Electric Veh. J.*, vol. 13, no. 1, 2021, Art. no. 6.
[17] X. Zhang, F. Liu, and T. Mei, "Multifrequency phase-shifted control for multiphase multiload MCR WPT system to achieve targeted power distribution and high misalignment tolerance," *IEEE Trans. Power Electron.*, vol. 36, no. 1, pp. 991–1003, Jan. 2021.
[18] A. K. Swain, S. Devarakonda, and U. K. Madawala, "Modeling, sensitivity analysis, and controller synthesis of multipickup bidirectional inductive power transfer systems," *IEEE Trans. Ind. Informat.*, vol. 10, no. 2, pp. 1372–1380, May 2014.
[19] X. Dai, C. Tang, Y. Sun, Z. Wang, and A. P. Hu, "Investigating a H∞ control method considering frequency uncertainty for CLC type inductively coupled power transfer system," in *Proc. IEEE Energy Convers. Congr. Expo.*, pp. 2022–2027, 2011.
[20] A. Hakemi, D. P. Jovanovic, D. M. Vilathgamuwa, G. R. Walker, and J. P. Pauls, "Generic uncertainty parameter analysis and optimization of series–series wireless power transfer system for robust controller design," *IEEE Trans. Ind. Electron.*, vol. 69, no. 4, pp. 4107–4118, Apr. 2022.
[21] Z. Zhang, H. Pang, A. Georgiadis, and C. Cecati, "H∞ mixed sensitivity robust control method of relay ICPT system for output voltage regulation," *Elect. Eng.*, vol. 103, no. 2, pp. 781–792, 2021.
[22] R. Isermann and M. Münchhof, *Identification of Dynamic Systems*. Berlin, Germany: Springer, 2011.
[23] P. C. Young, *Recursive Estimation and Time-Series Analysis: An Introduction*. Berlin, Germany: Springer, 2012.
[24] A. Zhu et al., "Modeling and phase synchronization control of high-power wireless power transfer system supplied by modular parallel multi-inverters," *IEEE Trans. Veh. Technol.*, vol. 70, no. 7, pp. 6450–6462, Jul. 2021.
[25] Q. Deng, P. Sun, W. Hu, D. Czarkowski, M. K. Kazimierczuk, and H. Zhou, "Modular parallel multi-inverter system for high-power inductive power transfer," *IEEE Trans. Power Electron.*, vol. 34, no. 10, pp. 9422–9434, Oct. 2019.

Shuaiqi Li received the B.S. degree in automation in 2019 from Wuhan University, Wuhan, China, where he is currently working toward the Ph.D. degree in control science and engineering with the School of Electrical Engineering and Automation.

His research interests include wireless power transfer systems and system identification.

Qijun Deng received the B.S. and M.Sc. degrees in mechanical engineering and the Ph.D. degree in computer application technology from Wuhan University, Wuhan, China, in 1999, 2002, and 2005, respectively.

In 2005, he joined the Department of Automation (which now is merged into School of Electrical Engineering and Automation), Wuhan University, where he is currently a Professor. From 2013 to 2014, he was a Visiting Scholar with the New York University Tandon School of Engineering, Brooklyn, NY, USA. His research interests include wireless power transfer, distribution automation, and electrical power informatics.

Zhifan Li received the B.S. degree in automation in 2019 from Wuhan University, Wuhan, China, where he is currently working toward the Ph.D. degree in control science and engineering with the School of Electrical Engineering and Automation.

His research interests include wireless power transfer systems, system identification and dc-dc converters.

Jiangtao Liu received the B.S. and M.Sc. degrees in control theory and applications and the Ph.D. degree in electrical engineering from Wuhan University, Wuhan, China, in 2003, 2010, and 2013, respectively.

In 2003, she joined the School of Physical, Mechanical and Electrical Engineering, Hubei University of Education, Wuhan, where she is currently a Professor. From 2013 to 2014, she was a Visiting Scholar with the New York University Tandon School of Engineering, Brooklyn, NY, USA. Her research interests include wireless power transfer and noise reduction for power transformers.

Chang Yu (Member, IEEE) received the Ph.D. degree in control science and engineering from Wuhan University, Wuhan, China, in 2020.

He is currently a Postdoctoral Researcher with the Postdoctoral Station of Control Science and Engineering, Wuhan University of Science and Technology. His research interests include distributed control, monitoring, and security in cyber-physical systems, and cooperation and optimization in smart microgrids.

Kaicong Cui received the B.S. degree in automation in 2021 from Wuhan University, Wuhan, China, where he is currently working toward the M.Sc. degree in electronic and information science with the School of Electrical Engineering and Automation.

His research interests include wireless power transfer and dc-dc converters.

Peng Luo received the B.S. degree in automation in 2021 from Wuhan University, Wuhan, China, where he is currently toward the M.Sc. degree in control theory and control engineering with the School of Electrical Engineering and Automation.

His current research interests include the areas of wireless power transfer.